# Supporting Information

## High-Performance Quasi-Solid-State Supercapacitor Based on CuO Nanoparticles with Commercial-Level Mass Loading on Ceramic Material $La_{1-X}Sr_XCoO_{3-\delta}$ as Cathode

Peipei Liu[†‡], Xiaolin Weng[†], Zhijun Liu[†], Yapeng Zhang[†], Qianyuan Qiu[†], Wei Wang[†], Mingyang Zhou[†], Weizi Cai[‡], Meng Ni[‡,*], Meilin Liu[†,§], Jiang Liu[†,*]

[†]*Guangzhou Key Laboratory for Surface Chemistry of Energy Materials, New Energy Research Institute, School of Environment and Energy, South China University of Technology, Guangzhou 510006, China.*

[‡]*Department of Building and Real Estate, The Hong Kong Polytechnic University, Hung Hom, Kowloon, Hong Kong China.*

[§]*School of Materials Science and Engineering, Georgia Institute of Technology, 771Ferst Drive, Atlanta, Georgia 30332-0245, United States.*

*Corresponding authors:

E-mail: meng.ni@polyu.edu.hk; jiangliu@scut.edu.cn.

**Table S1 *ESR* and $R_{ct}$ comparisons of LSC73, LSC64 and LSC55.**

| $x$ in $La_{1-x}Sr_xCoO_{3-\delta}$ | Sample | *ESR* ($\Omega$ cm$^2$) | $R_{ct}$ ($\Omega$ cm$^2$) |
|---|---|---|---|
| 0.3 | LSC73 | 1.25 | 0.41 |
| 0.4 | LSC64 | 1.17 | 1.37 |
| 0.5 | LSC55 | 1.13 | 2.43 |

Table S1 lists the *ESR* and $R_{ct}$ values of LSC73, LSC64 and LSC55. Though the *ESR* values are very close, the $R_{ct}$ values are greatly different. In order from greatest to least they are LSC55 > LSC64 > LSC73. The reason can be attributed to that the rhombohedral perovskite structure distorts gradually with the increase of Sr content ($x$) [1,2].

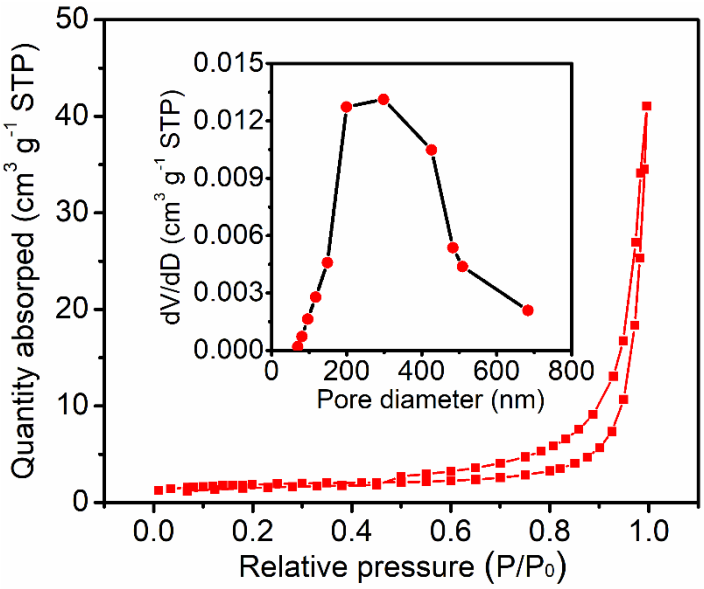


**Figure S1 Nitrogen adsorption-desorption isotherm and its corresponding pore size distribution profiles of the CuO/LSC73 nanocomposite.**

To further determine the porous structure of the CuO/LSC73, nitrogen adsorption-desorption measurement was carried out, as shown in Figure S1. The calculated effective surface area by BET is 6.12 $m^2$ $g^{-1}$. The pore size distributions center at~200 and 300 nm with a relative wide distribution at ~420 nm, which was estimated by BJH, confirming the macrostructure of CuO/LSC73.

The redox reaction of the active material CuO in 3.0 M KOH electrolyte is shown in equation S1 [3], as following:

$$2CuO + H_2O + 2e^- \leftrightarrow Cu_2O + 2OH^- \quad (1)$$

$$Cu_2O + H_2O + 2OH^- \leftrightarrow 2Cu(OH)_2 + 2e^- \quad (2)$$

$$CuOH + OH^- \leftrightarrow Cu(OH)_2 + e^- \quad (3)$$

$$CuOH + OH^- \leftrightarrow CuO + H_2O + e^- \quad (4)$$

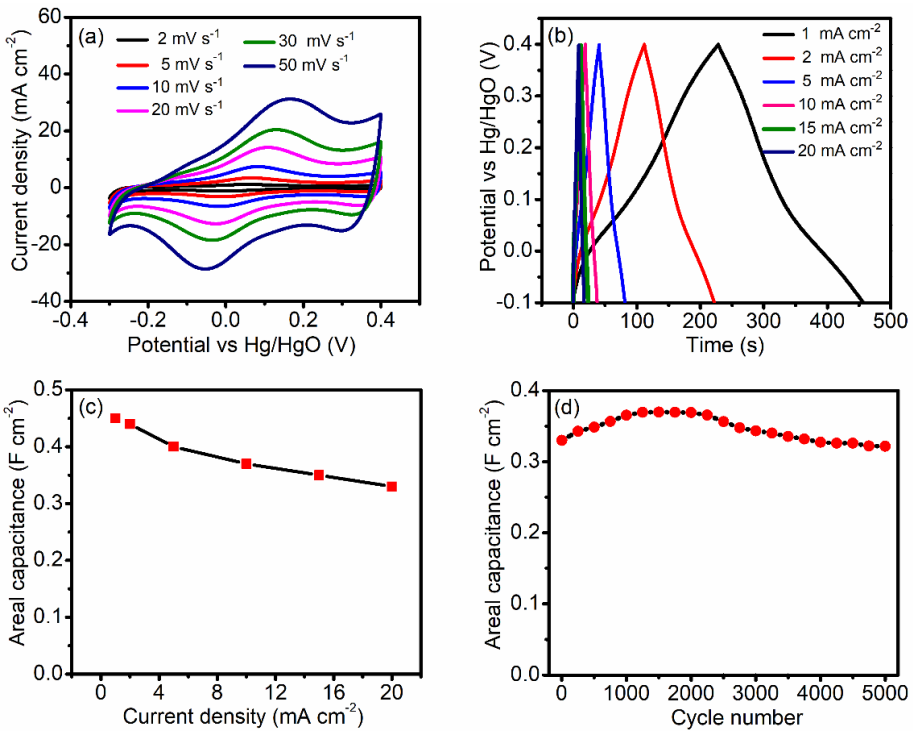


**Figure S2 Electrochemical behavior of the bare LSC73 electrode: (a) CV curves, (b) galvanostatic charge-discharge profiles, (c) areal capacitance at various current densities and (d) cycle stability at 20 mA cm$^{-2}$.**

Figure S2a presents the CV curves of the porous LSC73 substrate at scan rates from 2 to 50 mV s$^{-1}$. A pair of wide peaks can be seen, which is caused by the $Co^{3+}$ and $Co^{4+}$ in the LSC73. The galvanostatic charge-discharge curves are shown in Figure S2b. There are no obvious platforms, suggesting poor pseudocapacitive property of the bare LSC73 substrate. Figure S2c shows the evaluated areal capacitance of the substrate at various current densities. The obtained value is 0.45 F cm$^{-2}$ at 1 mA cm$^{-2}$, which is much lower than the CuO/LSC73 electrode (5.45 F cm$^{-2}$). Therefore, the capacitive contribution of LSC73 for the CuO/LSC73 electrode can be ignored. The long-term stability is carried out at 20 mA cm$^{-2}$, as shown in Figure S2d. Clearly, the initial capacitance retains as high as 97.5% after 5000 cycles, implying excellent stability of the porous LSC73 substrate.

**Table S2 Fitted resistances of CuO/LSC73 electrode.**

| Element | ESR | $R_{ct}$ | W1-R | W1-T | W1-P |
|---|---|---|---|---|---|
| Value ($\Omega$ $cm^2$) | 0.98 | 2.24 | 0.27 | 0.27 | 0.41 |

It is observed that the values of *ESR*, $R_{ct}$ and *W* are very small, as listed in Table S2, indicating low internal resistance, fast charge transfer and effective electrolyte ion diffusion of the CuO/LSC electrode [4, 5].

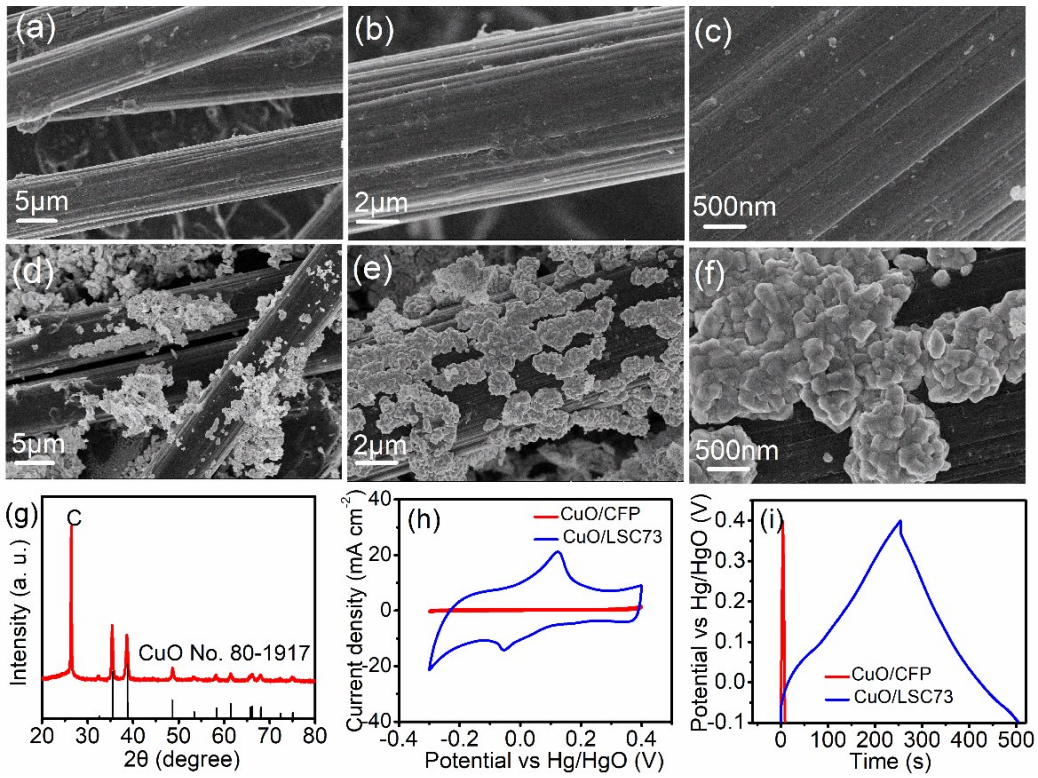


**Figure S3 SEM images of the (a-c) CFP and (d-f) CuO/CFP, (g) XRD pattern of the prepared CuO/CFP, (h) CV profiles at 2 mV $s^{-1}$ and (i) galvanostatic charge-discharge curves at 10 mA $cm^{-2}$ of CuO/CFP and CuO/LSC73.**

Figure S3a–c show the microstructure of the carbon fiber paper traditional substrate. There is almost no pore on the surface of the fiber, as displayed in Figure S3c. Active material CuO particles on CFP are seriously aggerated, as shown in Figure S3d–f, which is caused by the non-porosity and poor wettability of the CFP. The XRD pattern in Figure S3g confirms the high purity of the prepared CuO/CFP electrode. With the same mass loading of 10.0 mg $cm^{-2}$, CuO on LSC73 possesses larger enclosed area in the CV curve and longer discharge time in the GDC profile than CuO on CFP, as shown in Figure S3h and i, implying better capacitive performance of the CuO/LSC73.

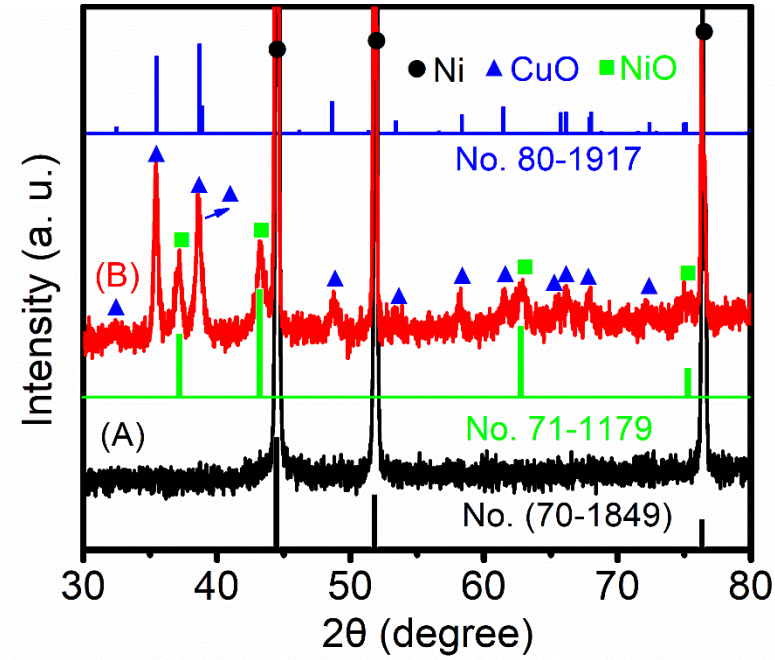


**Figure S4 XRD patterns of the bare Ni foam and CuO-NiO/Ni foam.**

The line (A) in Figure S4 shows the XRD patterns of the bare Ni foam. The peaks at 44.5º, 51.8º and 76.3º can be attributed to the (111), (200) and (220) planes of Ni foam (JCPDS No. 70-1849), respectively, which agree well with previously reported work. However, after input of the Ni foam into $Cu(NO_3)_2$ solution combined with subsequent Ar calcination treatment, both the diffraction peaks of CuO and NiO occurred in line B in Figure S4, implying the bare Ni foam is corroded by the $Cu(NO_3)_2$.

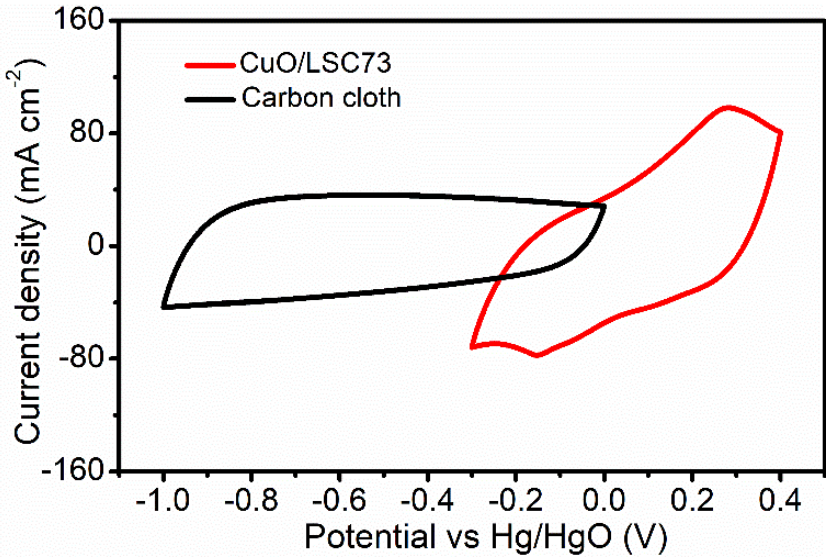


**Figure S5 CV curves of CuO/LSC73 and carbon cloth at a scan rate of 20 mV $s^{-1}$.**

Figure S5 shows the potential windows of CuO/LSC73 and carbon cloth are -0.3-0.4 V and -1-0 V, therefore it is expected that the operating voltage for the designed asymmetric supercapacitor can reach to 1.4 V. Moreover, the positive electrode and negative electrode must keep charge balance ($Q^+ = Q^-$) to obtain optimal performance for supercapacitor [6]. It is well known that the charge stored by each electrode depends on the specific capacitance ($C$), mass of active material ($m$) and potential window ($\Delta E$), as shown in the following Equation (1): [7]:

$$Q = C \times m \times \Delta E \qquad (1)$$

In order to obtain $Q^+ = Q^-$, the mass balance of the two electrodes should meet the following Equation (2):

$$\frac{m^+}{m^-} = \frac{C^- \times \Delta E^-}{C^+ \times \Delta E^+} \qquad (2)$$

Therefore, the optimal mass ratio between CuO/LSC73($m^+$) and carbon cloth ($m^-$) electrode is ~0.46.

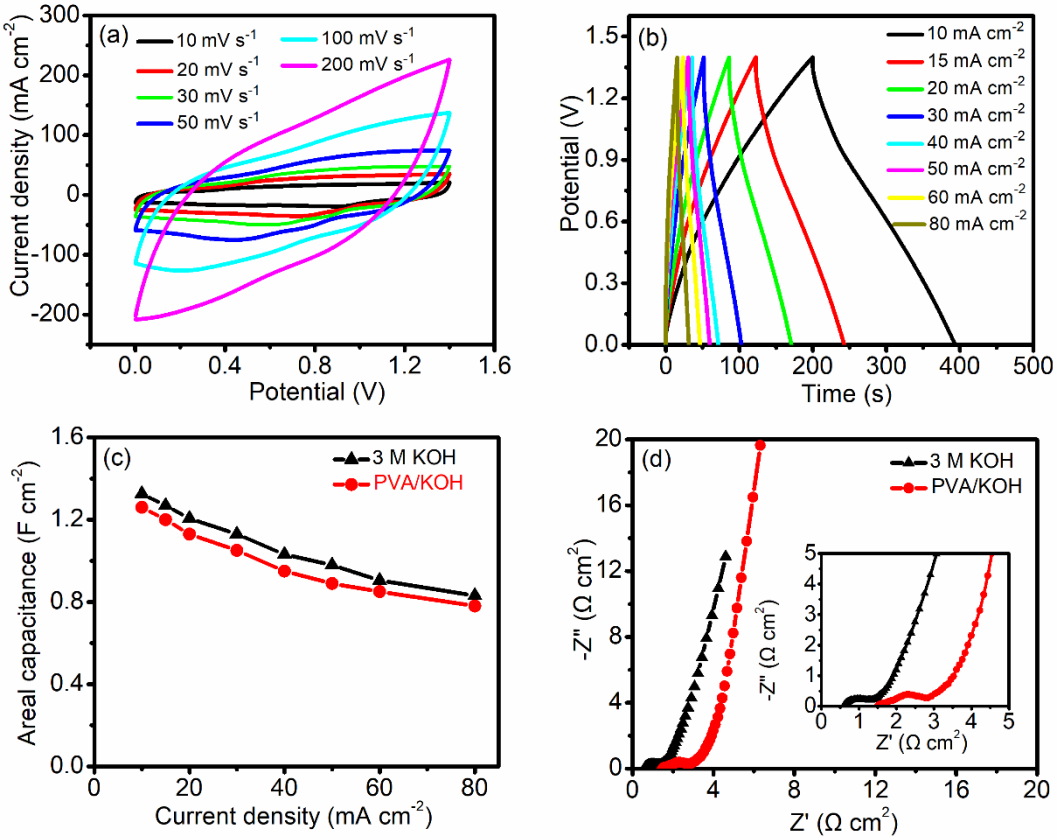


**Figure S6 Electrochemical behaviors of the aqueous asymmetric supercapacitor CuO/LSC73//CC: (a) CV curves at various scan rates and (b) galvanostatic charge- -discharge profiles at different current densities. Electrochemical performance comparison between aqueous and quasi solid-state devices: (c) areal capacitances and (d) electrochemical impedance spectra.**

Figure S6 a and b show CV curves at different scan rates and GDC profiles at various current densities of the CuO/LSC73//CC aqueous supercapacitor, respectively. No obvious redox peaks and charge-discharge platforms can be found, suggesting its capacitive nature. The areal capacitances of the aqueous and quasi solid-state device are compared, as exhibited in Figure S6c. Obviously, the quasi solid-state CuO/LSC73//CC supercapacitor with 3 M KOH and PVA/KOH as electrolyte shows comparable areal capacitance at various current densities that with 3 M KOH and PVA/KOH as electrolyte, respectively. The gap of the electrochemical impedance between aqueous and quasi solid-state device is shown in Figure S6d. It is seen that the

quasi solid-state supercapacitor presents slightly higher *ESR* (1.49 Ω $cm^2$) and $R_{ct}$ (1.42 Ω $cm^2$) than these of aqueous device (0.58 and 0.79 Ω $cm^2$), which can be ascribed to the inferior wettability and low ionic conductivity of the PVA/KOH gel [8-10].

## REFERENCES


[1] Gwon O.; Yoo S.; Shin J.; Kim G. Optimization of $La_{1-x}Sr_xCoO_{3-\delta}$ Perovskite Cathodes for Intermediate Temperature Solid Oxide Fuel Cells Through The Analysis of Crystal Structure and Electrical Properties. *Int. J. Hydrogen Energy* **2014,** *39,* 20806-20811.

[2] Cao Y.; Lin B. P.; Sun Y.; Yang H.; Zhang X. Q. Symmetric/Asymmetric Supercapacitor Based on The Perovskite-Type Lanthanum Cobaltate Nanofibers with Sr-Substitution. *Electrochim. Acta* **2015,** *178,* 398-406.

[3] Wang, G. L.; Huang, J. C.; Chen, S. L.; Gao, Y. Y.; Cao, D. X. Preparation and Supercapacitance of CuO Nanosheet Arrays Grown on Nickel Foam. *J. Power Sources* **2011,** *196*, 5756-5760.

[4] Shao, Y. L.; El-Kady, M. F.; Lin, C. W.; Zhu, G. Z.; Marsh, K. L.; Hwang, J. Y.; Zhang, Q. H.; Li, Y. G.; Wang, H. Z.; Kaner R. B. 3D Freeze-Casting of Cellular Graphene Films for Ultra-High-Power-Density Supercapacitors. *Adv. Mater.* **2016,** *28,* 6719–6726.

[5] Harilal, M.; Krishnan, S. G.; Pal, B.; Reddy, M. V.; Rahim, M. H. A.; Yusoff, M. M.; Jose R. Environment-Modulated Crystallization of $Cu_2O$ and CuO Nanowires by Electrospinning and Their Charge Storage Properties. *Langmuir* **2018,** *34*, 1873−1882.

[6] Yu, D. S.; Goh, K.; Zhang, Q.; Wei, L.; Wang, H.; Jiang, W. C.; Chen, Y. Controlled Functionalization of Carbonaceous Fibers for Asymmetric Solid-State Micro-Supercapacitors with High Volumetric Energy Density. *Adv. Mater.* **2014,** *26,* 6790–6797.

[7] Mohammadi, A.; Arsalani, N.; Tabrizi, G. A.; Moosavifard, S. E.; Naqshbandi, Z.; Ghadimi, L. S. Engineering rGO-CNT Wrapped $Co_3S_4$ Nanocomposites for High-Performance Asymmetric Supercapacitors. *Chem. Eng. J.* **2018**, *334*, 66–80.

[8] Xu J.; Wang Q. F.; Wang, X. W.; Xiang Q. Y.; Liang B.; Chen D.; Shen G. Z. Flexible Asymmetric Supercapacitors Based upon $Co_9S_8$ nanorod//$Co_3O_4$@$RuO_2$ Nanosheet Arrays on Carbon Cloth. *ACS NANO* **2013,** *7*, 5453–5462.

[9] Lu X.; Yu M.; Wang G.; Tong Y. X.; Li Y. Flexible Solid-State Supercapacitors: Design, Fabrication and Applications. *Energy & Environ. Sci.* **2014,** *7,* 2160-2181.

[10] Fan H. L.; Liu W.; Shen W. Z. Honeycomb-Like Composite Structure for Advanced Solid State Asymmetric Supercapacitors. *Chem. Eng. J* **2017,** *326*, 518-527.